J Mater Sci (2006) 41:4554–4560
DOI 10.1007/s10853-006-0086-8

Contribution of dynamic charging effects into dopant contrast mechanisms in silicon

Yuli Chakk · Dror Horvitz

Received: 1 December 2005 / Accepted: 7 March 2006 / Published online: 28 June 2006
© Springer Science+Business Media, LLC 2006

Abstract In this work, SEM capability for imaging of both p- and n-doped regions in Si was demonstrated. The best dopant contrast was found when the primary electron range (R) is comparable or larger than the maximum escape depth of secondary electrons (~5λ) (λ stands for mean free path). Beyond this scale ($R < 5\lambda$, $R >> 5\lambda$) the contrast between p-, n-doped and intrinsic regions gradually disappears. The dopant profiles obtained by SEM were judged using scanning capacitance microscopy (SCM), dopant selective etch (DSE) and secondary ion mass spectrometry (SIMS) measurements, and excellent matching was demonstrated. A novel dopant contrast mechanism incorporating *dynamic* charging effects that take place during e-beam/specimen interaction is suggested. Under threshold steady-state imaging conditions, an E_{bi} field in Si near the surface region is formed. This field, governed by secondary electron (SE) emission and trapping of some incident and generated SE, accelerates electrons towards the surface in p-type regions and decelerates them in n-type regions, compared with the intrinsic material. This results in the observed dopant contrast: $C(n) < C(i) < C(p)$. Use of the SEM for 2D-dopant imaging provides many advantages; giving fast results, covering a wide range of dopant concentrations, applicable to real devices, and does not require sample preparation needed by SCM and DSE. In addition, SEM-dopant contrast data quantification is possible using SIMS standards which needs to be defined with more details.

Y. Chakk (✉) · D. Horvitz
Intel Electronics Ltd., P. O. Box 100, Kiryat Gat 82109, Israel
e-mail: yuli.chakk@intel.com

Introduction

Performance of semiconductor devices strongly depends on the doping type and level, the position of p–n junctions and the channel length. With the shrinkage of modern semiconductor devices to deep submicron levels, a great need exists for direct dopant profile measurements with sub-10 nm spatial resolution, 10% accuracy, and sensitivity to dopants over the 10^{16}–10^{20} cm^{-3} range, as defined by the Semiconductor Industry Association (SIA) [1]. Such measurements are a subject of considerable research activity in the semiconductor community since they can give rapid feedback for developing and improving the performance of devices and control of the manufacturing process.

The ability to distinguish regions of different doping type and concentration has been a uniquely difficult problem. The extreme requirements, as set by the SIA, have stimulated the development of numerous carrier profiling analytical techniques. These techniques can be divided into four major categories: (1) SIMS (secondary ion mass spectrometry); (2) chemical DSE (dopant selective etching); (3) SPM (scanning probe microscopy) techniques like SCM (scanning capacitance microscopy), and (4) electron microscopy-based techniques like SEM (scanning electron microscopy).

However, each of the above techniques has some restrictions with respect to the most important features like spatial resolution, dynamic range, sensitivity, quantification ability and applicability to real devices. For example, SIMS is recognized as the best method for dopant quantification in a very broad dynamic range. However, this technique provides only 1D-information, and is not applicable to real devices, requiring special test structures [2].

The DSE technique uses mixtures of HF and an oxidizing agent to preferentially etch regions with a high

carrier concentration [3]. This etching followed by imaging with AFM or SEM is valuable for fast qualitative analysis of the 2D carrier profile [4, 5]. However, there are some limitations: poor control of the etching conditions causes poor reproducibility; lack of quantification procedure; the PMOS devices etch differently from the NMOS; and the reaction mechanisms of the etching are still not completely understood [6, 7].

The SCM is a powerful technique to analyze 2D-carrier profiling with a required dynamic range. It can also be applied on arbitrary structures, and approaches a resolution close to the values required by the SIA [7]. However, sample preparation may introduce some undesired artifacts caused by the use of an ion beam (e.g., Ga^+), polishing, and oxide growth. This may result in the difference between the metallurgical and electrical p-n junctions known as carrier spilling [8]. SCM images clearly vary with V_{bias}, changing the junction location [9]. Additionally, quantification accuracy and reproducibility are still issues which need to be studied in more detail [7, 10, 11].

Recently, the ability of using a SEM electron probe for 2D-carrier analyses was demonstrated, mostly for p-doped materials: p-doped regions appear brighter than n-doped [12]. It was also shown that the SE intensity is sensitive to the doping concentration levels [13, 14]. Since then, there has been much debate regarding the dopants contrast mechanism. Among the suggested models are: p–n junction built-in potential, surface-band bending, vacuum level variation outside the semiconductor, and others [14–17]. However, these models are insufficient since they mainly treat the contrast mechanism as a *static* phenomenon. Additionally, the effect of the instrumental parameters on the dopant contrast mechanism is still poorly understood.

In this work, the ability of SEM for imaging of both p- and n-doped regions in silicon was demonstrated over a wide dopant range. Differently doped substrates were characterized by SEM as a function of several parameters: accelerating voltage, electron-beam current and dwell time, doping type and dose, and substrate surface conditions. As a result, optimal imaging conditions capable of distinguishing between different dopants were established. A new dopant contrast mechanism incorporating *dynamic* charging effects that take place during e-beam/specimen interaction was suggested.

Experimental details

Patterned and blanked p–n junctions were fabricated in (100) oriented p- and n-doped silicon wafers. Dopant concentrations within the 10^{16}–10^{20} cm^{-3} ranges were used. The penetration depth of the dopants was controlled by implant energy.

The samples were cleaved in air along a direction perpendicular to the [001] to expose a {110} plane. The freshly cleaved cross section samples with p-n junctions were immediately loaded into a Hitachi S4800 field emission SEM and the following imaging parameters were examined: accelerating voltages of 0.2–30 keV; emission currents of 1–20 μA, and a wide range of dwell times, working distances, etc. The electron beam probe current in the 1.5 pA–0.6 nA range was measured using a Faraday cup for fixed-aperture and spot-size settings. These data were used for Monte Carlo simulations and other numerical estimations required for understanding the dopant contrast mechanism. All the images were acquired with a through-the-lens upper secondary electron detector.

Dopant profiles imaged by SEM were studied using several complementary analytical techniques such as SCM, SIMS, and chemical DSE followed by SEM. SCM measurements were performed with a Digital Instruments Dimension 5000 AFM/SCM using commercially available PtIr AFM probes. Conventional polishing and surface-bake techniques were used to prepare the sample surface prior to imaging. Depth profiles of differently doped samples were accomplished by SIMS using the Cameca 6F spectrometer. The DSE samples were prepared using combined etching solutions of 49% HF, 98% HNO_3, and CH_3OOH. The sample topography after the etching was imaged by SEM.

Results

Typical SEM micrographs of differently doped silicon regions captured at 1 keV are shown in Fig. 1. Differences in contrast between p- and n-doped regions are clearly distinguished: p-doped areas (boron implant) appear brighter than n-doped regions (phosphorus implant).

The dependence of the dopant contrast on SEM imaging conditions such as accelerating voltage, emission current, dwell time, working distance and others were investigated. It was found that the yield of SE from differently doped regions is mostly affected by the accelerating voltage, while the effect of the others is of second order. The best contrast was obtained for the accelerating voltage of 0.5–2 keV. Above and below these values, the dopant contrast gradually disappears (see Fig. 2).

Validation of the dopant profile features (e.g., shapes, dimensions, etc.) was performed using SCM, SIMS, and chemical DSE techniques. Figure 3 compares SEM and SCM images. The images indicate that both methods reveal similar contrast features between differently doped regions. Intrinsic boron (B)- and phosphorus (P)-doped regions can be distinguished. For SEM images, B-doped areas appear as bright regions, intrinsic areas are of intermediate

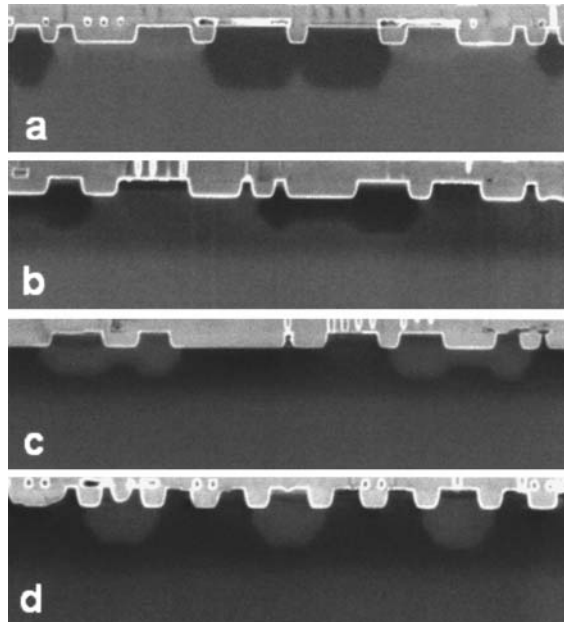

Fig. 1 Examples of cross-section SEM images showing contrast differences between n- (**a**), (**b**) and p-doped regions (**c**), (**d**). Note that the p-doped areas appear brighter than the n-doped regions

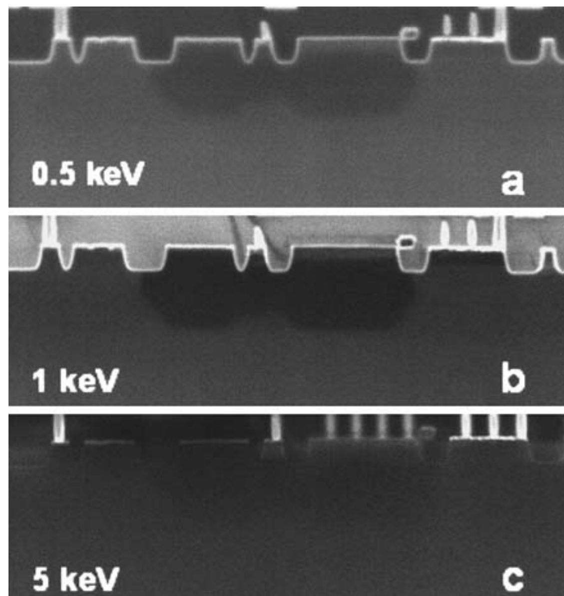

Fig. 2 SEM images showing dependence of the dopant contrast on the acceleration voltage: (**a**) 0.5 keV; (**b**) 1 keV; (**c**) 5 keV. The best contrast was observed for an accelerating voltage of ~1 keV. The dopant contrast gradually disappears above and below this value. All the images were captured from the same location

intensity, while P-doped regions are the darkest: $C(\text{n}) < C(\text{i}) < C(\text{p})$.

An example of using the DSE recipe for dopant decoration is shown in Fig. 4. As can be seen, the dopant profiles obtained using selective etch are similar to those

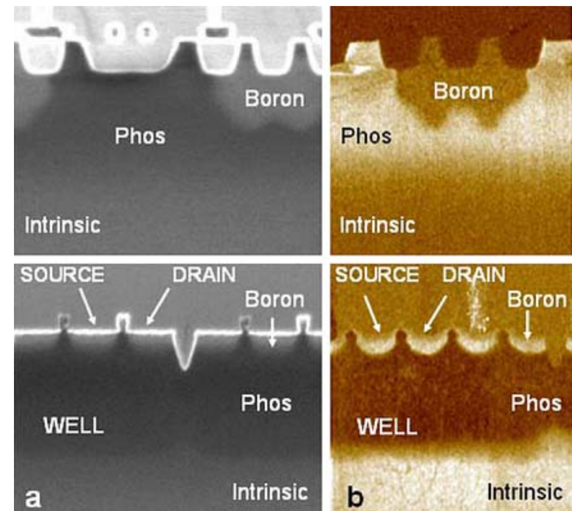

Fig. 3 Comparison of dopant profiles obtained by (**a**) SEM with (**b**) complementary SCM analyses. SEM and SCM images were captured from the identical structures. Both methods reveal similar contrast features between differently doped regions: Intrinsic, boron- and phosphorus-doped regions are distinguished

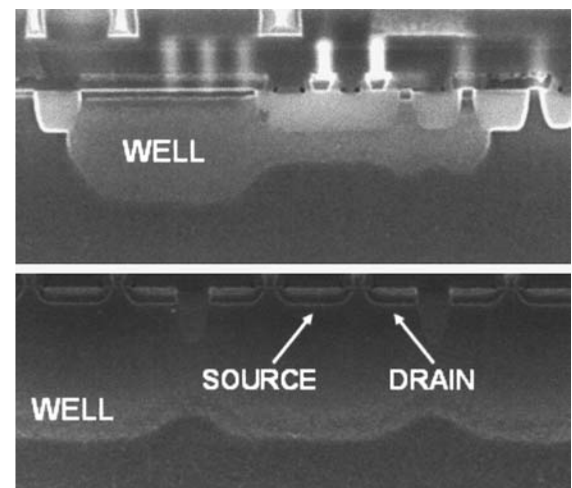

Fig. 4 SEM images showing dopant decoration profiles as they appear after dopant selective etch (DSE) recipe

observed by SEM imaging (see Fig. 1 and 3a for comparison).

Additionally, SIMS dopant profile measurements were performed to verify dimensions of the doped areas as they appear by SEM (see Fig. 5a, b). The same depth dimensions were measured by both methods. Figure 5c shows a SE intensity profile extracted from the cross-sectional SEM image presented at Fig. 5a. By comparing the image intensity data to a 1D profile obtained by SIMS, the relation between the intensity and dopant concentration can be found. From this comparison, dopant dose quantification using SIMS standards could be possible with further research.

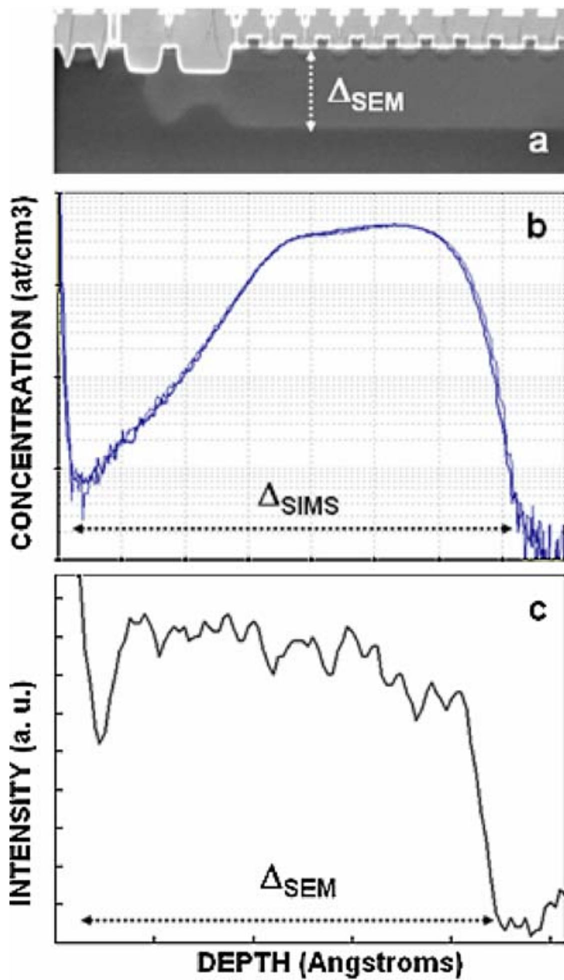

Fig. 5 Verification of the dopant profile dimensions as obtained by (**a**) SEM compared with (**b**) SIMS measurements. Note that the same dopant depths were measured by both methods; (**c**) example of SE intensity profile extracted from the cross sectional SEM image

From all the above, use of the SEM electron beam is a powerful tool to visualize both p- and n-dopants. The dopant profiles observed by SEM are in good agreement with the other existing methods; SCM, SIMS and DSE. Use of SEM for dopant imaging provides fast results, does not require the sample preparation needed by SCM and DSE, is applicable to real devices, and covers a wide range of dopant concentrations.

Discussion

Constant loss approximation (CLA) for SE yield

The proposed dopant contrast mechanism is based on the results described above. It is known that the three main processes which contribute to SE emission from the surface are: (1) electron production within the material; (2) migration of the electrons to the surface; and (3) escape of the SE over the surface potential barrier [18, 19]. The first two processes strongly depend on the bulk properties, while the third process depends on surface properties (see Fig. 6a).

From the above, the SE yield (δ) can be described as follows:

$$d\delta = n(z, E_0)P_{\mathrm{m}}(z)P_{\mathrm{e}}dz \tag{1}$$

where $n(z, E_0)dz$ represents a number of SE produced by incident energy E_0 in the layer of thickness dz at a depth z below the surface; $P_{\mathrm{m}}(z) = \exp(-z/\lambda)$ is a migration probability to the surface from a depth z, and λ stands for the mean free path (MFP); and $P_{\mathrm{e}} = B$ is the escape probability.

According to the constant-loss approximation [18–20], the primary energy dissipation within the material is approximately constant, the number of primary electrons (PE) would decrease linearly to a depth R, and the number of SE produced per unit path length would be a constant. For this approach

$$n(z, E_0) = -(1/\xi)(dE/dz) = (1/\xi)(E_0/R) \tag{2}$$

where (is the energy required to excite one SE inside the solid and R is the maximum range of the PE.

From Eq. (1) and (2), the total SE yield can be expressed as

$$\delta = B(E_0/\xi)(\lambda/R)\{1 - \exp[-(R/\lambda)]\} \tag{3}$$

where the integral from the surface ($z = 0$) to the primary electron range ($z = R$) is evaluated. As Eq. 3 indicates, the SE yield depends on several parameters: the maximum PE range; the number of SE generated within the interaction volume; the mean free path of the SE, and their escape probability B. Qualitatively, such dependence results in a graph as shown in Fig. 6b where the dependence of R on E_0 is taken into account [18].

Effect of accelerating voltage of PE on dopant contrast in Si

During the irradiation of Si by the primary electron beam, electrons experience energy losses where the dominant mechanism is the excitation of the valence-band electrons towards the conduction band. This inelastic process leads to electron–hole (e–h) pair generations which may occur up to the maximum penetration depth of the incident electrons R. The carriers generated inside the interaction volume undergo several processes: partially escape from the surface, diffuse away from the generation region, undergo recombination, and become partially trapped.

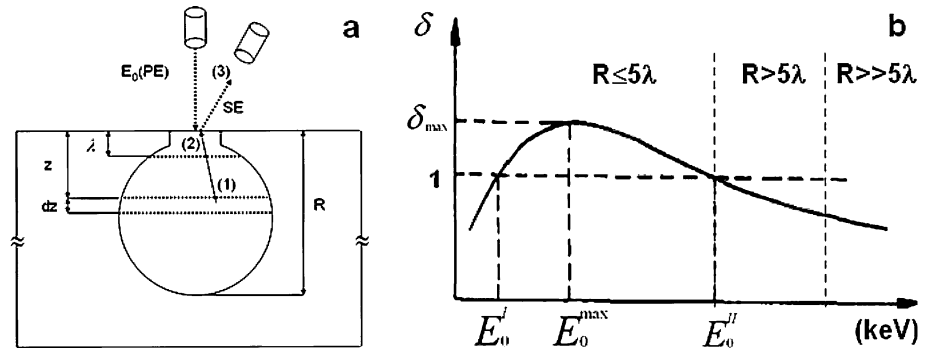

Fig. 6 (**a**) Schematic representation of three main processes which contribute to SE emission: (1) electron production within the material; (2) migration of the electrons to the surface, and (3) escape of the SE over the surface potential barrier; (**b**) dependence of SE yield δ on PE energy E_0; the main e-beam/Si interaction parameters are summarized in Table 1

Under steady-state SEM imaging conditions, substrate charging effects can take place. These effects mostly result from a *dynamic* competition between SE emission and trapping of some PE or generated SE. SE emission contributes to a positive charging, while PE/SE trapping contributes to a negative charging.

Dependence of the Si interaction volume on PE beam energy as obtained by Monte Carlo simulation is shown in Fig. 7a. It was estimated that the volume dimensions can vary from ~10 nm for 0.5 keV to several microns for 30 keV. In contrast, the maximum escape depth T of the SE is independent of the PE beam energy and does not exceed $T \sim 5\lambda$ [21]. For Si, this value is $T \sim 3.8$–5.4 nm [22]. Some other Si parameters mentioned in Eq. 3 and Fig. 6b are summarized in Table 1.

From the above, three different cases can be distinguished: (a) $R > 5\lambda$, (b) $R \leq 5\lambda$, and (c) $R > > 5\lambda$ (see Fig. 7b). In (a), when $R > 5\lambda$, two distinct regions inside the interaction volume can be considered: a thin near-surface layer with thickness $T \sim 5\lambda$ and positive charge Q^+, and a negatively charged bulk with thickness ~(R–T) and Q^-. As a result, the implanted charge is $\Delta Q = Q^+ + Q^-$, and the electric field E_{bi} governed by ΔQ builds up. This field can modify the parameters involved in the generation and the escape probability of the SE, as well as modifying the parameters governing the trapping and detrapping of the PE.

For Si, case (a) approximately covers ~0.5 keV < E_0 < 2 keV acceleration voltages, as estimated by Monte Carlo simulations. This range of E_0 values is the most favorable for the dopant contrast, as shown above. The sign of ΔQ is slightly negative as deduced from Table 1 and Fig. 6b. process 1 appear. The sign of ΔQ may change depending on the charge balance between injection and emission processes. This approximately corresponds to E_0 < 0.5 keV accelerating voltage values (see Fig. 6b process 2). Below this lower threshold value, the dopant contrast gradually disappears.

In contrast to case (b), case (c) $R > > 5\lambda$ is similar to case (a) $R > 5\lambda$ qualitatively. Two distinct regions inside

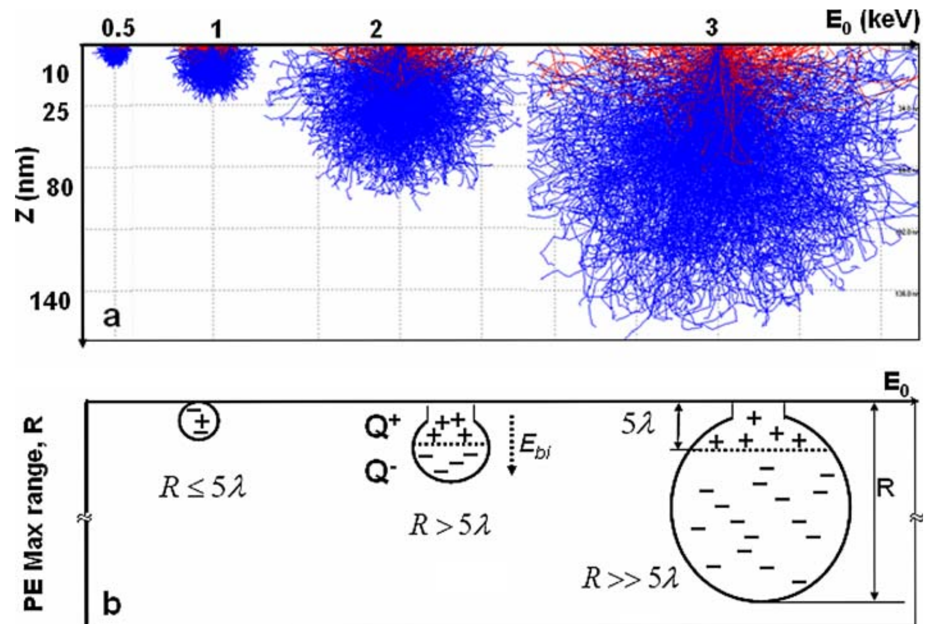

Fig. 7 (**a**) Dependence of Si interaction volume on PE beam energy as obtained by Monte Carlo simulation; (**b**) Sketch of the charge distribution inside Si interaction volume plotted against maximum PE range (R) and max SE escape depth (~5λ). Three different cases can be distinguished: $R > 5\lambda$, $R \leq 5\lambda$, and $R \gg 5\lambda$

Table 1 Summary of the main e-beam/Si interaction parameters (see Fig. 6 and Eq. 3 for more details) [16, 21, 22]

	E_I (keV)	E_{II} (keV)	E_{max} (keV)	δ_{max}	λ (nm)	$\xi = E_{eh}$ (eV)
Si	0.125	0.5	0.25–0.3	0.9–1.1	1.5–2.2	3.4

the interaction volume still can be considered. However, gradual increase of the PE range above the upper threshold value should affect the densities of the injected and generated charges. This should influence the E_{bi} value in the near-surface region.

Typical densities of injected and generated charges affecting E_{bi} values can be estimated. The electron–hole pair generation rate G_{eh} inside the interaction volume created by the PE energy beam, E_0, and the current I is

$$G_{eh} = I(E_0/E_{eh})/\frac{4}{3}\pi r^3 \quad (4)$$

where E_{eh} is energy required to create one e–h pair, (E_0/E_{eh}) is a number of e–h pairs generated by a single primary electron of E_0, and r is the radius of the interaction volume. For Si, a 15 keV beam of 10 pA generates ~10^{21} pairs/cm^3, assuming E_{eh} ~ 3.4 eV (see Table 1). Since the PE range $R \sim E_0^{1.75}$ [18], the generation rate increases rapidly with decreasing R. For example, for 1 keV and the same beam current, 10 pA, this value reaches ~10^{27} pairs/cm^3. Thus, the typical SEM beam is capable of creating a rather enormous number of carriers inside the interaction volume of Si.

Under fixed SEM imaging conditions, the steady-state population of the charges is smaller due to the SE escape, carrier diffusion, recombination and trapping. As Fig. 6b shows, higher keV results in a larger amount of the implanted charge ΔQ relative to the low-keV case. However, charge density at a low keV is larger then a high keV. Higher charge density is favorable for higher E_{bi} values, and vice versa. For case (c), the upper threshold value for the accelerating voltage is ~2 keV. Above this value, the dopant contrast disappears, as confirmed experimentally.

Dopant contrast mechanism in Si

For the established window of E_0 providing maximum dopant contrast (case (a)), impact of E_{bi} on the SE escape probability B can be evaluated (see Eq. 3). In order to escape from the surface, the SE has to overcome the affinity barrier ((see Fig. 8a). An electron escaping from Si (media with ϵ_r ~ 12) and moving in the vacuum (ϵ ~ 1), experiences two forces: external electric field E_{ex} applied between the substrate and the SE collector, and the force exerted by its own image set in Si (the electric image effect) [23, 24]. As a result, on the vacuum side of the interface, there is a Schottky barrier lowering $\Delta\chi$ which takes the form:

$$\Delta\chi = -q\sqrt{qE_{ex}K/\varepsilon_0} \quad (5)$$

where $K = (\varepsilon_r - 1)(\varepsilon_r + 1)$, and q is an electron charge.

The extra E_{bi} field in the near-surface region accelerates electrons towards the surface in addition to the electric field applied between substrate and the SE collector. This results in formation of the effective field $E_{ef} = E_{ex} + \alpha E_{bi}$ (see Fig. 8b curve I). For intrinsic Si, the parameter $\alpha = 1$ is assumed. For the p-doped region, the presence of positive ions increases the positive charge of the near-surface area, resulting in $\alpha > 1$ (Fig. 8b curve II). In contrast, for the n-doped region, $\alpha < 1$, that decreases the value of the E_{ef} as compared to both, intrinsic and p-doped values (Fig. 8b curve III). The parameter α is dose dependent which needs to be investigated in more detail.

From the above, E_{ef} accelerates the SE in the p-type region relative to the intrinsic area, and decelerates them in the n-type. This results in the Schottky barrier lowering/thinning for p-doped Si relative to the intrinsic region. On the other hand, there is a barrier increasing/broadening for the n-doped material, as compared to the intrinsic area. All of this results in the observed SEM contrast sequence: $C(n) < C(i) < C(p)$.

Contrast dose sensitivity in the SEM can be explained as follows. The positioning of the Fermi level in p- and n-doped Si relative to the intrinsic regions can be obtained from:

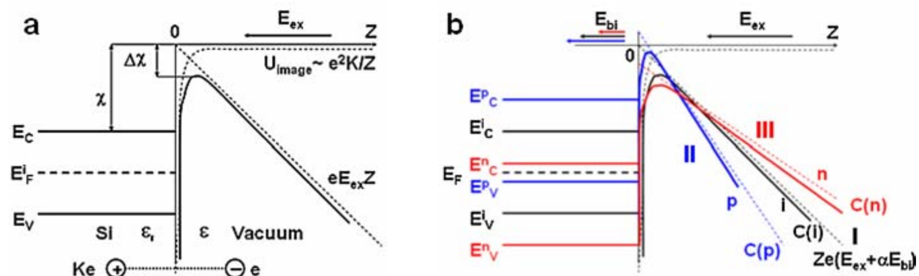

Fig. 8 (**a**) Sketch of a Schottky barrier lowering $\Delta\chi$ caused by external electric field applied between the substrate and SE collector, and the electric image effect; (**b**) Combined sketch of band structures for intrinsic, p- and n-doped regions in the same specimen

$$E_F - E_i = kT\ln(n/n_i) = -kT\ln(p/n_i) \quad (6)$$

where E_F and E_i are Fermi levels in intrinsic and doped materials, n_i is an intrinsic carrier density, n and p are the doping levels, and T is temperature [25].

For n-type Si, a dose increase shifts the Fermi level towards the edge of the conduction band. In the case of p-type Si, there is a downward shift in the Fermi level. These upward/downward shifts, as dictated by Eq. (6), are dependent on the extrinsic dopant dose. For example, a change of the dopant dose from 10^{16} cm^{-3} to 10^{20} cm^{-3} at room temperature results in the corresponding E_F shift of ~0.25 eV, ($n_i \sim 10^{10}$ cm^{-3} is assumed). The aforementioned changes in the Si band structure also either facilitate or inhibit the SE yield, contributing to the dopant contrast observed between p- and n-doped regions.

Conclusions

Using SEM for imaging both p- and n-doped regions in Si was demonstrated. The best contrast between differently doped Si areas was obtained for ~0.5–2 keV accelerating voltage. Beyond these values, the contrast between p-, n-doped, and intrinsic regions gradually disappears. The impact of the rest of the imaging parameters on dopant contrast is of a second order. The dopant profiles obtained by SEM were compared using complementary SCM, chemical DSE and SIMS measurements, and excellent matching was demonstrated.

A novel mechanism describing doping-dependent image contrast is suggested. The mechanism incorporates *dynamic* charging effects that take place during e-beam/specimen interaction and appears to be as follows. Primary e-beam/silicon interaction generates electron–hole pairs within the interaction volume. These carriers partially escape from the surface, diffuse away from the generation region, undergo recombination, and become partially trapped, resulting in the charging. Under steady-state imaging conditions, this results in a charge distribution within the interaction volume, and this plays a crucial role in dopant contrast mechanism.

The most favorable case for dopant contrast is when the PE range (R) is comparable or higher than the maximum SE escape depth (5λ). Beyond this scale ($R < 5\lambda$ or $R \gg 5\lambda$) the contrast between p- and n-doped regions disappears. This observation is described by formation of the E_{bi} field in the near-surface region of Si which is governed by *dynamic* competition between SE emission contributing to a positive charging and the trapping of some PE or generated SE responsible for a negative charging.

This field accelerates SE towards the surface of the p-type region, and decelerates them in n-type. In turn, this results in the Schottky barrier lowering/thinning for p-doped Si relative to the intrinsic material. On the other hand, the barrier increasing/broadening takes place for n-doped Si, as compared to the intrinsic one. All this reveals the observed SEM contrast sequence: C(n) < C(i) < C(p).

Use of the SEM for dopant imaging provides fast results, does not require the sample preparation needed by SCM and DSE, covers a wide range of dopant concentrations, and is applicable to real devices. In addition, dopant contrast data quantification using SIMS standards could be possible with further research.

Acknowledgement The authors wish to thank E. Kaganer for the SIMS measurements and I. Vidoshinsky for his help with the dopant selective etching recipe development.

References

1. National Technology Roadmap for Semiconductors (1997) Semiconductor Industry Association, San Jose, CA
2. Dowsett MG (1997) In: Gillen G, Larea R, Bennet J, Steve F (eds) Proceedings of the SIMS XI Conference. Wiley, Chichester
3. Barrett M, Dennis M, Tiffin D, Li Y, Shih K (1995) IEEE Electron Device Lett 16:118
4. Gong L, Petersen S, Frey L, Ryssel H (1995) Nucl Instrum Methods Phys Res B 96:133
5. Neubauer G, Lawrence M, Dass A, Johnson TJ (1992) Mater Res Soc Symp Proc 286:283
6. Mahaffy R, Shih K, Edwards H (2000) J Vac Sci Technol B 18(1):566
7. De Wolf P, Stephenson R, Trenkler T, Clarysse T, Hantschel T, Vandervorst W (2000) J Vac Sci Technol B 18(1):361
8. Duhayon N, Clarysse T, Eyben P, Vandervorst W, Hellemans L (2002) J Vac Sci Technol B 20(2):741
9. Smoliner J, Basnar B, Golka S, Gornik E, Loffler B, Schatzmayr M, Enichlmair H (2001) Appl Phys Lett 79(19):3182
10. O'Malley ML, Timp GL, Moccio SV, Garno JP, Kleiman RN (1999) Appl Phys Lett 74(2):272
11. Stephenson R, De Wolf P, Trenkler T, Hantschel T, Clarysse T, Jansen P, Vandervorst W (2000) J Vac Sci Technol B 18(1):555
12. Perovich DD, Castell MR, Howie A, Lavoie C, Tiedje T, Cole JSW (1995) Ultramicroscopy 58:104
13. Venables D, Jain H, Collins DC (1998) J Vac Sci Technol B 16(1):362
14. Schonjahn C, Broom RF, Humphreys CJ, Howie A, Mentink SAM (2003) Appl Phys Lett 83(2):293
15. Sealy CP, Castell MR, Wilshaw PR (2000) J Electron Micros 49(2):311
16. Mullerova I, El-Gomati MM, Frank L (2002) Ultramicroscopy 938:223
17. El-Gomati MM, Wells TCR (2001) Appl Phys Lett 79(18):2931
18. Joy DC (1987) J Microsc 147(1):51
19. Dionne GF (1973) J Appl Phys 44(12):5361
20. Lye RG, Dekker AJ (1957) Phys Rev 107(4):977
21. Seiler H (1983) J Appl Phys 54(11)
22. Seiler H (1967) Z Angew Physik 22:249
23. Landau L, Lifshitz EM (1960) Electrodynamics of continuous media. Pergamon, Oxford
24. Cazaux J (1999) J Electron Spectroscopy and Rel Phenomena 105:155
25. Pierret RF (1996) Semiconductor device fundamentals. Addison Wesley Longman